

## Article

# Nanocrystalline Cellulose Supported MnO<sub>2</sub> Composite Materials for High-Performance Lithium-Ion Batteries

Quang Nhat Tran <sup>1</sup>, Thuan Ngoc Vo <sup>1</sup> , Il Tae Kim <sup>1</sup> , Ji Hyeon Kim <sup>1</sup>, Dal Ho Lee <sup>2</sup> and Sang Joon Park <sup>1,\*</sup>

<sup>1</sup> Department of Chemical and Biological Engineering, Gachon University, Seongnam 13120, Gyeonggi-do, Korea; tran.nhat147@gachon.ac.kr (Q.N.T.); vnthuanbk@gmail.com (T.N.V.); itkim@gachon.ac.kr (I.T.K.); jihyeon@gachon.ac.kr (J.H.K.)

<sup>2</sup> Department of Electronics Engineering, Gachon University, Seongnam 13120, Gyeonggi-do, Korea; dhlee@gachon.ac.kr

\* Correspondence: psj@gachon.ac.kr; Tel.: +82-31-750-5358; Fax: +82-31-750-5363

**Abstract:** The rate capability and poor cycling stability of lithium-ion batteries (LIBs) are predominantly caused by the large volume expansion upon cycling and poor electrical conductivity of manganese dioxide (MnO<sub>2</sub>), which also exhibits the highest theoretical capacity among manganese oxides. In this study, a nanocomposite of nanosized MnO<sub>2</sub> and pyrolyzed nanocrystalline cellulose (CNC) was prepared with high electrical conductivity to enhance the electrochemical performance of LIBs. The nanocomposite electrode showed an initial discharge capacity of 1302 mAh g<sup>-1</sup> at 100 mA g<sup>-1</sup> and exhibited a high discharge capacity of 305 mAh g<sup>-1</sup> after 1000 cycles. Moreover, the MnO<sub>2</sub>-CNC nanocomposite delivered a good rate capability of up to 10 A g<sup>-1</sup> and accommodated the large volume change upon repeated cycling tests.

**Keywords:** manganese dioxide; nanocrystalline cellulose; lithium-ion batteries; nanocomposite; discharge capacity



**Citation:** Tran, Q.N.; Vo, T.N.; Kim, I.T.; Kim, J.H.; Lee, D.H.; Park, S.J. Nanocrystalline Cellulose Supported MnO<sub>2</sub> Composite Materials for High-Performance Lithium-Ion Batteries. *Materials* **2021**, *14*, 6619. <https://doi.org/10.3390/ma14216619>

Academic Editor: Cai Shen

Received: 2 October 2021

Accepted: 2 November 2021

Published: 3 November 2021

**Publisher's Note:** MDPI stays neutral with regard to jurisdictional claims in published maps and institutional affiliations.



**Copyright:** © 2021 by the authors. Licensee MDPI, Basel, Switzerland. This article is an open access article distributed under the terms and conditions of the Creative Commons Attribution (CC BY) license (<https://creativecommons.org/licenses/by/4.0/>).

## 1. Introduction

Recently, rechargeable lithium-ion batteries (LIBs) with metal oxide-based materials, such as iron oxide, tin dioxide, cobalt oxide, titanium dioxide, manganese dioxide, and nickel oxide, have attracted significant interest as anodes. LIBs owing metal oxide anode materials are promising due to their favorable chemical properties and high performance [1–10]. A wide range of transition metal oxides, sulfides, selenides, fluorides, nitrides, and phosphides have been approached as conversion-type anode materials (CTAMs) for LIBs, which greatly increase the materials for high performance LIBs. Furthermore, many CTAMs are found in their natural forms and have low production costs in comparison with alloying-type anode materials. In addition, compared to graphite anodes with a low Li-intercalation potential, CTAMs show better safety of LIBs by avoiding the problem of lithium dendrite formation. Moreover, silicon-based and phosphorous (P) materials coated with magnesium (Mg) may be considered to be promising for Li metal as an anode and cathode for the large market of next generation LIBs, and could be a replacement for graphite and graphitic carbon as electrode materials [11–15]. One of the transition metal oxides and conversion-type anode materials, manganese dioxide (MnO<sub>2</sub>), is not only the most stable form of MnO<sub>x</sub> compounds but also shows the highest theoretical capacity of 1232 mAh g<sup>-1</sup> among manganese oxides. MnO<sub>2</sub> is particularly attractive as an electrode material in LIBs because of its high energy density, small voltage hysteresis, high abundance, low conversion potential, and environmental friendliness [9,16–23]. However, drawbacks, such as poor electrical conductivity and large volume expansion during charge-discharge cycling, limit the performance of LIBs. The poor electrical conductivity causes poor rate capability, and the large volume expansion during cycling significantly affects the battery stability [16,24]. This limitation results in a significant drop in the capacity

at high current densities. Many approaches have been proposed, such as the synthesis of nanostructured  $\text{MnO}_2$ , to overcome these problems and to achieve improved battery performance [16,17,25–27].

The size and the morphology of nanostructured  $\text{MnO}_2$  particles are beneficial for improving the contact area between the electrode and the electrolyte, to prevent structural distortion caused by  $\text{Li}^+$  insertion/extraction, and to reduce the diffusion pathways of Li ions. However, the high surface energy of metal nanoparticles leading to self-aggregation could decrease the productive contact area between the conductive additives, electrolyte, and active materials [28]. Moreover, side reactions between the active materials (owing to their high surface area) and the electrolyte shorten the cycle life of the battery and raise safety concerns [28]. Forming a nanocomposite with electrically conductive carbon additives is a valid method to overcome the poor electrical conductivity of  $\text{MnO}_2$  [9,25,26,29–37]. Among the carbon-based materials, pyrolyzed nanocrystalline cellulose (CNC) not only maintains the structural stability of anode materials, but also enhances the electrical conductivity of  $\text{MnO}_2$ , owing to its excellent colloidal stability [37,38]. Furthermore, CNC is uniformly dispersed in solution owing to the presence of negative surface charges; this prevents the aggregation of metal oxide nanoparticles during the synthesis process [39]. The low cost, light weight, and favorable physicochemical robustness of CNCs are expected to enable their wide commercial applications.

In this work, we prepared  $\text{MnO}_2$ -CNC nanocomposite with porous nanosized  $\text{MnO}_2$  to exploit the low external surface area and the low surface energy of nanostructured particles, and could prevent side reactions and self-aggregation. Pyrolyzed CNC enhances the electrical conductivity of the anode nanocomposite and also alleviates stress due to volume changes to improve the material electrochemical performance during the cyclability. Moreover, pyrolyzed carbon material effectively prevents nanoparticle aggregation and acts as a dispersant for the synthesis of nanosized  $\text{MnO}_2$ . Thus, the  $\text{MnO}_2$ -CNC nanocomposite is expected to be a promising electrode material to provide improved capacity and the stable cycle performance of LIBs.

## 2. Materials and Methods

### 2.1. Materials

The CNC suspension obtained from SK Innovation Co. Ltd. (Daejeon, Korea) was pyrolyzed at 800 °C (as described in our previous paper [40]) and was used as a source of CNC for synthesizing the nanocomposite from  $\text{MnO}_2$  and CNC. Manganese (II) sulfate hydrate ( $\text{MnSO}_4 \cdot x\text{H}_2\text{O}$ ) and potassium permanganate ( $\text{KMnO}_4$ ), purchased from Sigma-Aldrich Co. Ltd. (St. Louis, MO, USA), were used in this study.

### 2.2. Synthesis of $\text{MnO}_2$ -CNC Nanocomposite

The  $\text{MnO}_2$ -CNC nanocomposite was prepared by a modified approach, as previously described [31]. Specifically, 0.2 g of pyrolyzed CNCs was dispersed in 35 mL (10 mM) of  $\text{MnSO}_4$  by ultrasonication for 10 min. The obtained suspension was maintained at a controlled temperature of 80 °C, and was magnetically stirred for 20 min. Then, 150 mL of aqueous solution of (33 mM)  $\text{KMnO}_4$  was heated at 80 °C and gradually added to the previous mixture. The resulting suspension was stirred under a controlled temperature of 80 °C for 15 min. The obtained sample was washed, filtered, and dried at 100 °C for 10 h.

### 2.3. Materials Characterization

The nanocomposite materials were characterized using an X-ray diffractometer (XRD) (Rigaku/Smartlab, Tokyo, Japan) operated at 40 kV and 30 mA with a  $\text{K}\beta$  filter for Cu. The XRD profile was examined with a scan rate of  $5.0^\circ \text{ min}^{-1}$  from 10 to  $80^\circ$  for  $2\theta$  angle. The structural and morphological characterizations of the samples were examined by using scanning electron microscopy (SEM; S-4700, Hitachi Ltd., Tokyo, Japan) and transmission electron microscopy (TEM; Tecnai, F30S-Twin, Hillsboro, OR, USA), and elemental maps were obtained by energy dispersive X-ray analysis (EDX). Thermogravimetric analysis

(TGA) was applied for analyzing the composition of the nanocomposite with a temperature increase rate of  $10\text{ }^{\circ}\text{C min}^{-1}$  under atmospheric condition. Brunauer–Emmett–Teller (BET) specific surface areas of  $\text{MnO}_2\text{-CNC}$  composites were determined by  $\text{N}_2$  adsorption at 77.3K (Micromeritics, ASAP 2020).

#### 2.4. Electrochemical Performance Measurement

To produce the working electrode (mass loading of  $0.088\text{ mg/cm}^2$ ), a slurry containing 70 wt% of the nanocomposite as active materials, 15 wt% Poly(vinylidene fluoride) (PVDF), 15 wt% Super P, and N-methyl pyrrolidone, was prepared and coated on a Cu foil ( $r = 0.6\text{ cm}$ ). The electrodes were maintained at  $60\text{ }^{\circ}\text{C}$  for 3 h and then dried overnight at  $70\text{ }^{\circ}\text{C}$  in a vacuum oven. The electrochemical performance of the obtained  $\text{MnO}_2\text{-CNC}$  nanocomposite was directly evaluated using coin cells (CR2032) fabricated in a glove box filled with argon. The cells consisted of a coin cell base, a polyethylene membrane as the separator, a plastic ring, a lithium foil as the counter electrode, a spacer, a coin spring for improving contact and the coin cell lid. A mixture of ethylene carbonate/diethylene carbonate (1:1 in volume) dissolved with 1 M  $\text{LiPF}_6$  was used as the electrolyte solution (see Figure 1). Cyclic voltammetry (CV) were tested from 0.01 to 3.0 V at a scan rate of  $0.1\text{ mV s}^{-1}$ . The battery cycler (WBCS3000, WonAtech) system was used to examine the cell performance experiments and cycle performance tests under a constant current density of  $100\text{ mA g}^{-1}$  at 0.01–3.0 V (vs.  $\text{Li/Li}^+$ ) at room temperature. Subsequently, the rate performance tests were performed using various current densities in the range  $100\text{--}10,000\text{ mA g}^{-1}$ .

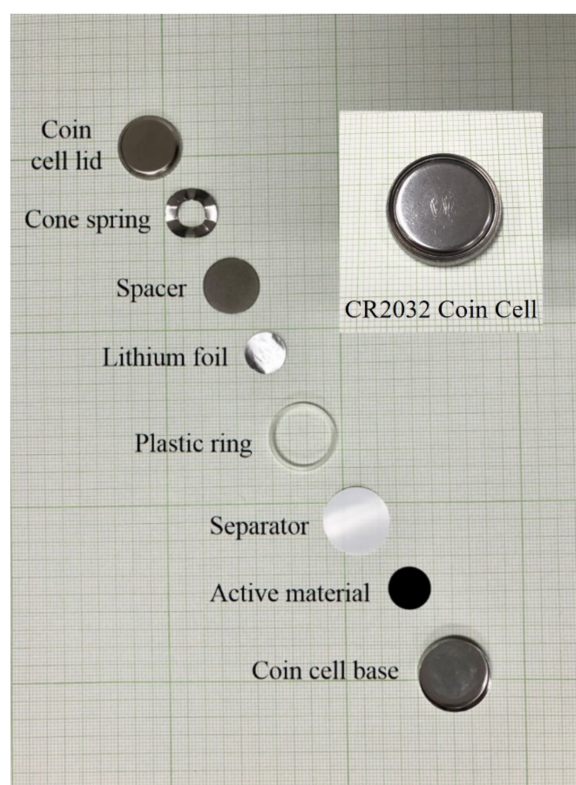


Figure 1. The component of the testing LIB coin cell.

### 3. Results and Discussion

Figure 2a shows the XRD pattern of CNC. The obtained peaks are centered at  $19.8$ ,  $22.6$ ,  $34$ , and  $40.2^{\circ}$ , which match well with the data provided by SK Innovation Co. Ltd. The presence of sharp peaks designates the crystalline nature of CNC. The XRD profile of  $\text{MnO}_2\text{-CNC}$  nanocomposite in Figure 2b shows the characteristic peaks of native cellulose and cellulose at  $19.5$ ,  $27.7$ ,  $31$ ,  $34.8$ , and  $41.4^{\circ}$ , which totally agrees with the ICSD data (PDF 03-0289 and 03-0226). The peaks centered at approximately  $15.8$ ,  $22.8$ ,  $25$ ,  $32$ ,  $36.9$ ,

and  $52.7^\circ$  correspond to the (110), (002), (002), (220), (400), and (002) planes, respectively, of  $\epsilon$ - $\text{MnO}_2$  (ICSD PDF 12-0141). The peaks of  $\text{MnO}_2$  are sharper and more intense than those of CNC, indicating the formation of crystal phases  $\epsilon$ - $\text{MnO}_2$  and the coexistence of nanocrystalline phases (CNC) in the composite [30]. This is beneficial for increasing the electrical performance of the metal oxide electrode of the battery. The nanocrystalline phase is also expected to prevent the combination of nanosized  $\text{MnO}_2$  particles and to improve the contact between the electrode materials and the electrolyte, emerging in favorable cycle performance.

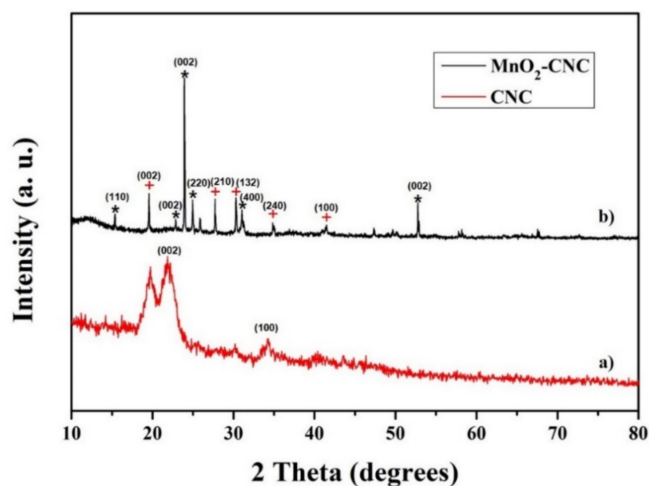


Figure 2. Powder XRD characteristic of (a) CNC and (b)  $\text{MnO}_2$ -CNC nanocomposite.

TGA was used to examine the chemical composition of the  $\text{MnO}_2$ -CNC nanocomposite. The TGA patterns of CNC and  $\text{MnO}_2$ -CNC nanocomposite are shown in Figure 3. The TGA curve of CNC shows a mass loss of approximately 7% below  $250^\circ\text{C}$ , corresponding to impurities and adsorbed water present in the air. The pyrolysis of CNC is recognized by the major weight loss between  $250$  and  $750^\circ\text{C}$  [40]. The extant material weight is 20.5%, which is considered to be that of pyrolyzed CNC. The TGA curve of the  $\text{MnO}_2$ -CNC composite shows a weight loss of 17% below  $250^\circ\text{C}$ , corresponding to adsorbed water, trace amounts of oxygen, and easily oxidizable matter present in the air. The weight loss gradually decreases from  $250$  to  $750^\circ\text{C}$ , which is believed to be due to the burning of CNC in air [41]. A residual weight of 68% is obtained for the  $\text{MnO}_2$ -CNC composite. Therefore, the mass percentage of residual  $\text{MnO}_2$  is calculated to be 47.5%.

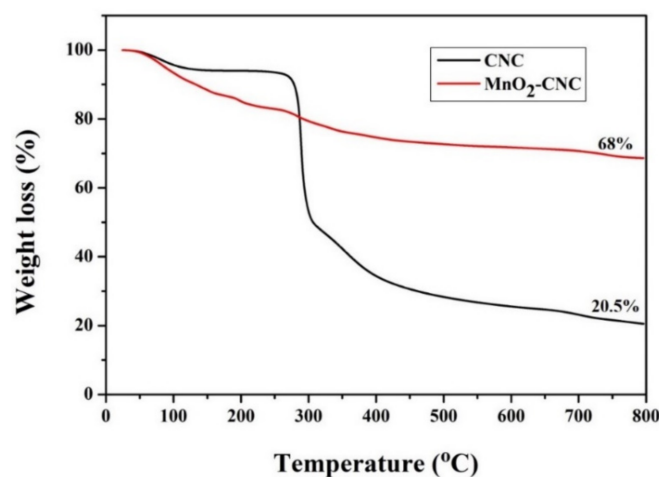
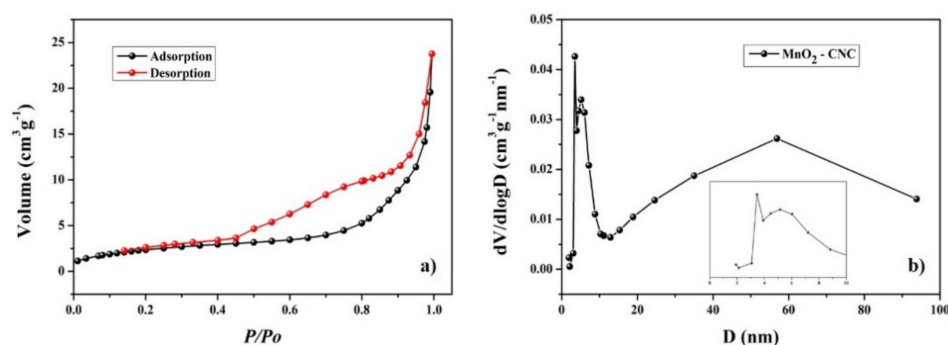


Figure 3. TGA curves of CNC and  $\text{MnO}_2$ -CNC composite.

The porous surface property of composite was determined by  $N_2$  isothermal adsorption and desorption, and the obtained results are shown in Figure 4. The pattern shows a typical IV isotherm curve with hysteresis loops, indicating the mesoporous structure of the composite [42]. The BJH adsorption and desorption average pore diameter are 17.56 and 10.85 nm, respectively. A wide hierarchical pore size distribution centered at 3.4 nm, 5.1 nm, and 56.9 nm could offer more approachable active sites for the intercalation of Li ion and electrochemical reaction to enhance the specific capacity of the electrode. On the other hand, the uniformly dispersed  $MnO_2$  on the CNC can effectively reduce the aggregation of  $MnO_2$  nanoparticles and also the mesoporous structure can prevent the volume expansion of  $MnO_2$ , which improves the cycling stability of the electrode [43].



**Figure 4.** (a) Nitrogen adsorption-desorption isotherm and (b) BJH pore size distribution of the composite.

The SEM system was used to study the surface morphology of the  $MnO_2$ -CNC nanocomposite, and the images are shown in Figure 5. The composite exhibits a uniform hierarchical structure consisting of  $MnO_2$  nanoparticles (Figure 5a). The hierarchical morphology of nanocomposite was recorded by high-magnification SEM image (Figure 5b), clearly confirming that the surface of the nanocomposite is porous. This indicates that  $MnO_2$  is covered by CNC, which prevents aggregation of nano-sized  $MnO_2$  and improves the electrode performance.

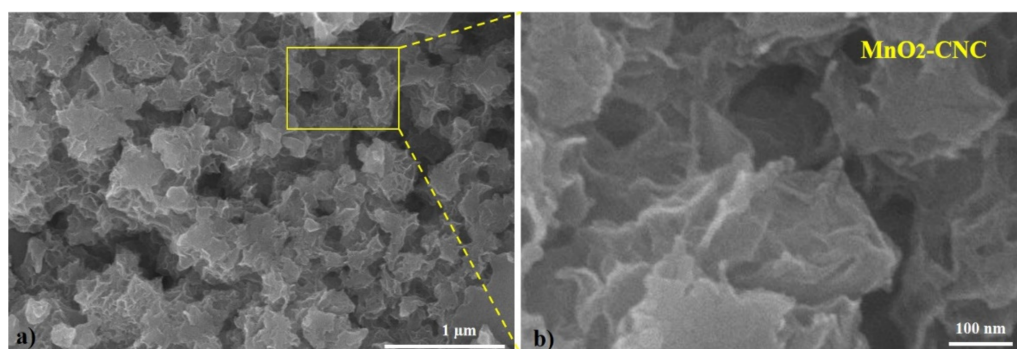


**Figure 5.** (a) Typical and (b) high-magnification SEM images of the  $MnO_2$ -CNC nanocomposite.

The more detailed morphology and nanostructure of the  $MnO_2$ -CNC nanocomposite were investigated by TEM and high-resolution TEM (HRTEM). Figure 6a,b indicate the obtained  $MnO_2$ -CNC nanocomposite exhibits uniformly distributed  $MnO_2$  nanoparticles covered with CNC, which is in accordance with the SEM results. The  $MnO_2$  nanoparticles exhibited an average particle size of 20–25 nm with a flower-shape. Moreover, the nanocomposite is efficiently segregated from the supporting CNC layer. The crystalline structure of  $MnO_2$  is evident from Figure 6c. The (400) and (002) planes of  $MnO_2$  are consolidated by lattice fringe spacings of 0.242 and 0.495 nm, respectively, which consistently agrees with the XRD results. The HRTEM images also showed the presence of a macroporous layer of the carbon substrate surrounding the  $MnO_2$  nanoparticles. Hence, the combination of the crystalline structure of nano-sized  $\epsilon$ - $MnO_2$  and the porous surface modification by CNC

in the MnO<sub>2</sub>-CNC nanocomposite is expected to extend and improve the cycling stability, rate performance, and initial reversible capacity of the nanocomposite, used as electrode materials in LIBs. Furthermore, the presence of MnO<sub>2</sub> particles and CNC in the nanocomposite is confirmed by the peaks from the EDX spectrum (Figure 6d), which corresponds to Mn, O, and C. The TEM elemental mapping of the MnO<sub>2</sub>-CNC nanocomposite, as shown in Figure 7, further confirmed the uniform distribution of MnO<sub>2</sub> and CNC.

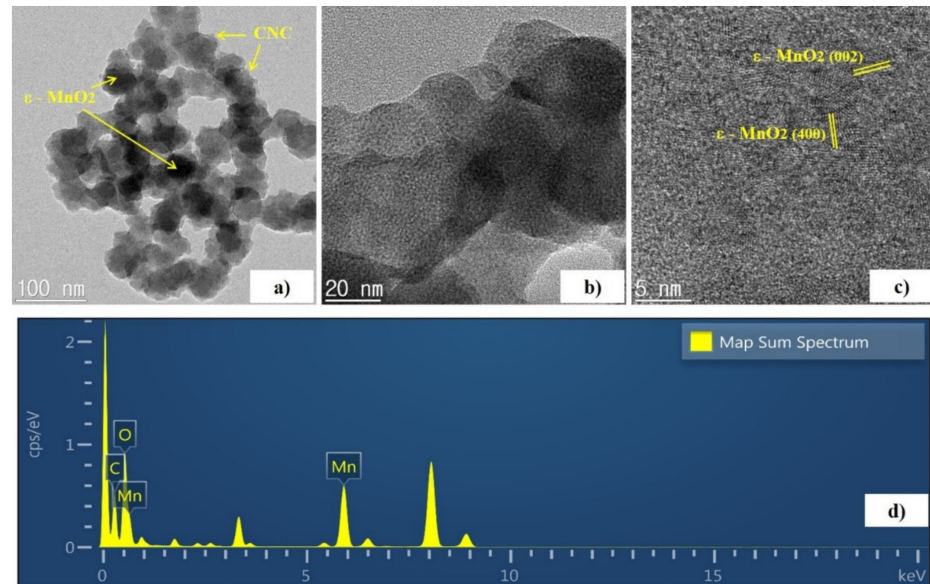


**Figure 6.** (a) Typical, (b,c) high-magnification TEM images and (d) EDX pattern of MnO<sub>2</sub>-CNC nanocomposite.

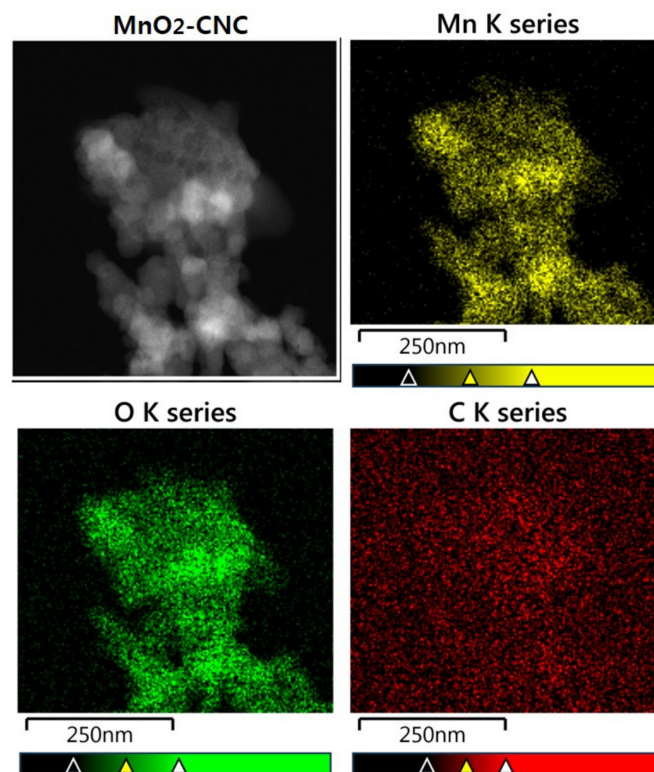


**Figure 7.** TEM elemental mapping of the MnO<sub>2</sub>-CNC nanocomposite.

A potential range 0.01–3.00 V was applied in LIBs to investigate the electrochemical properties of the MnO<sub>2</sub>-CNC nanocomposite, performed as an anode material. The discharge and charge capacities and the long-term cycle performance test of the MnO<sub>2</sub>-CNC nanocomposite electrode are shown in Figure 8a. The experiment tests were carried out at 100 mA g<sup>-1</sup> for 1000 cycles. Except for a significant decrease in the capacity during the first five cycles and a slight reduction in the stability over the next 100 cycles, the capacity increases to a steady value of approximately 300 mAh g<sup>-1</sup> in the subsequent thousand cycles. The nanocomposite exhibits an enhancement capacity of 30% compared to the obtained result at the 100th cycle with a good capacity of 305 mAh g<sup>-1</sup> after 1000 cycles. In addition, the charge–discharge capacity of the nanocomposite tends to a gradual increase in the cycle after decreasing in the first cycles; this is a characteristic phenomenon for metal-oxide nanocomposite anodes [9,44–48]. The pulverization of the nanocomposite during the lithiation process decreases the typical initial capacity, and the metal oxides' interfacial storage mechanism, resulting from the activation process on cyclability causing an increase in the capacity. Despite the loss of crystallinity of the nanosized MnO<sub>2</sub> particles during the cyclability process of anode nanocomposites, the incorporated CNC was more tolerant and flexible than the metal oxide structure, which helped the nanocomposite material anode to easily accommodate volume changes during lithiation and increase the capacity after cycling [34–39]. Thus, the nanocomposite electrode material exhibited a good stable property on cyclability, delivered a reversible capacity of 305 mAh g<sup>-1</sup> after 1000 cycles, and retained 36% of its inception capacity with a Coulombic efficiency of over 99.0%, which establishes a significant stable effective impact on the cyclability of nanocomposite. These results again confirm the supporting role of CNC, which minimizes the volume expansion to prevent the collapse of the MnO<sub>2</sub> structure, as a result of charging and discharging over many cycles.

A different current density range of 0.1, 0.2, 0.5, 1, 2, 5, and 10 A g<sup>-1</sup> was applied to examine the rate performance and charge and discharge capacity of the MnO<sub>2</sub>-CNC nanocomposite. Figure 8b shows the obtained results from the test. The nanocomposite electrode owns average reversible capacities of 492, 324, 279, 239, 210, 195, and 193 mAh g<sup>-1</sup>, respectively, for five cycles. Following the rate capability test, the specific applied current of 100 mA g<sup>-1</sup> is maintained for the next 10 cycles, and the electrode average capacity within 10 cycles increases to a value of 403 mAh g<sup>-1</sup>, indicating the stability and good rate-cycling performance of the electrode at various current densities.

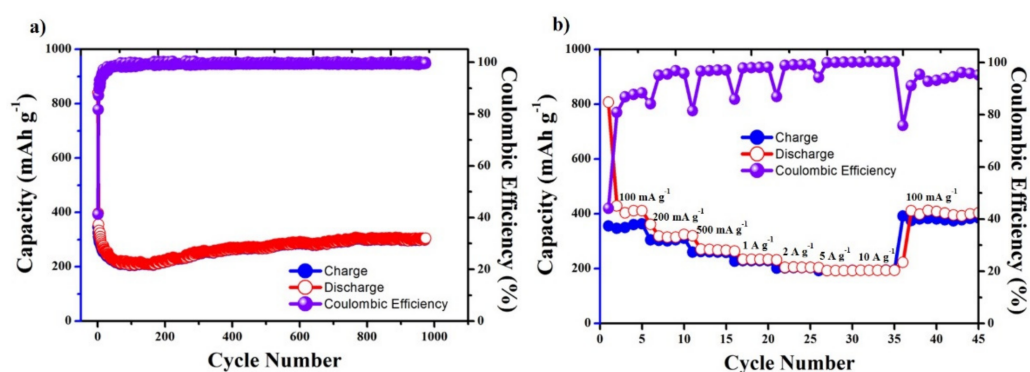


**Figure 8.** (a) Cyclic performances of the MnO<sub>2</sub>-CNC nanocomposite electrodes at 100 mA g<sup>-1</sup> and (b) Rate performance of MnO<sub>2</sub>-CNC nanocomposite electrodes at various current densities ranging from 0.01 V to 3 V.

The CV curves of three initial cycles from 0.01 to 3.0 V range at a scan rate of 0.1 mV s<sup>-1</sup> are shown in Figure 9. It can be clearly observed that the first CV curve shape and composite area differ from those of the next two cycles. On the first cathodic cycle, there is no peak that can be observed; however, in the following anodic process, there appears a significant peak at 1.15 V corresponding to the oxidation of MnO<sub>2</sub> nanoparticles during the delithiation reactions. From the second cycle, a reduction peak at 0.12 V can be confirmed,

indicating that the carbon-based materials may form a stable SEI film [37–40]. Moreover, a boarder oxidation peak can still be observed at 1.15 V from the second cycle and is almost overlapped, which suggests that MnO<sub>2</sub>-CNC has a good stability in structure and electrochemical property after the first cycle.

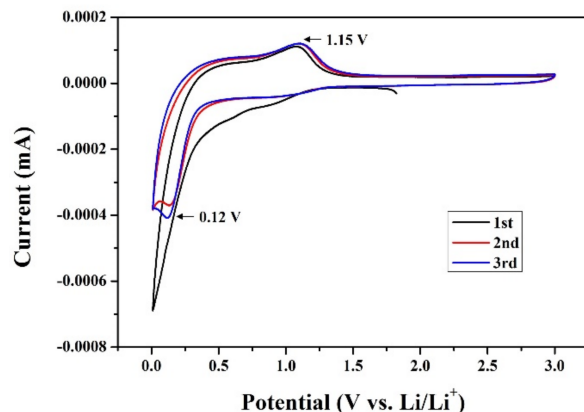


**Figure 9.** The Cyclic voltammetry (CV) curves of MnO<sub>2</sub>-CNC nanocomposite electrodes.

Figure 10a,b respectively show the typical charge–discharge capacities of the obtained nanocomposite electrode during cycling at a current density of 100 mA g<sup>−1</sup> and at different current densities in the potential range 0.1–3.0 V (Li/Li<sup>+</sup>). The initial charge capacity and discharge capacity of the nanocomposite electrode are 1302 and 398 mAh g<sup>−1</sup>, respectively. The corresponding initial Coulombic efficiency is 30%. However, these capacity values are superior to the theoretical capacities of MnO<sub>2</sub> and CNC. This phenomenon can be explained by the increase in the irreversible capacity of the electrode, caused by the decomposition of the electrolyte during the first discharge process and the formation of a solid–electrolyte interface (SEI) layer on the surface. Moreover, the supporting role of pyrolyzed CNC in the nanocomposite also contributes to the superior initial capacities [37,40]. The obvious discharge platform observed at approximately 0.7 V during the first discharge process, which can be recognized from Figure 10a, is attributed to the decomposition of the electrolyte and the formation of the SEI film. In the subsequent cycles, the platform at 0.7 V disappears, demonstrating that the SEI film is stably formed after the the first cycle. In addition, the electrodes’ irreversible capacity decreases significantly during the first cycle, which is a typical phenomenon in LIBs based on metal oxides. Furthermore, the charge and discharge profiles of the 2nd, 3rd, 100th, and 500th cycles show similar shaped curves. The trend in the reversible capacity of the nanocomposite after 500 cycles is similar to that after the 100th cycle, indicating that the nanocomposite material exhibits good electrochemical stability and stable operation cyclability from the second cycle.

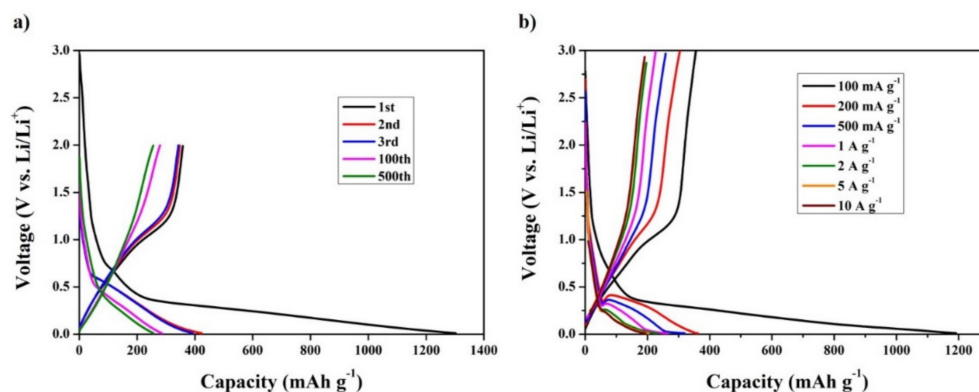


**Figure 10.** The charge–discharge profiles of the MnO<sub>2</sub>-CNC nanocomposite at (a) 100 mA g<sup>−1</sup> and at (b) various current densities.



Figure 10b shows the initial discharge–charge profiles of nanocomposite electrode at different current rates. The recorded capacities are 1191, 361, 319, 263, 231, 204, and 193 mAh g<sup>-1</sup> at 0.1, 0.2, 0.5, 1, 2, 5, and 10 A g<sup>-1</sup> current densities, respectively. At low current densities, the plateaus around 0.4 V during the discharge process and at approximately 1.25 V during the charging process are observed, which are similar to those observed in Figure 10a for the cycling test. At higher current rates, the plateaus in the charging process disappear, but the plateau in the discharge process is maintained, which evidences that electrochemical redox reactions mainly influence the lithium storage process at high current densities. However, the shapes of the discharge–charge pattern are representative of the conversion reactions of transition metal oxide-based electrodes, and the same shape is maintained at diverse current densities. This further demonstrates the favorable performance of the nanocomposite material at high current rates.

To further investigate the cycling influence on active material properties, SEM, TEM images, and XRD composite result after 1000 cycles were obtained and are shown in Figure 11. It can be observed from SEM and TEM images (Figure 11a,b) that the electrode could not maintain the good material structure and the aggregation appears after 1000 cycles. However, the porous structure and the carbon surrounding the MnO<sub>2</sub> nanoparticles could be observed after 1000 cycling, which again confirms that CNC still covers and reduces the aggregation and volume expansion of MnO<sub>2</sub>. Moreover, the XRD result (Figure 11c) shows that broader and clear peaks correspond to the appearance of CNC and MnO<sub>2</sub> nanoparticles.

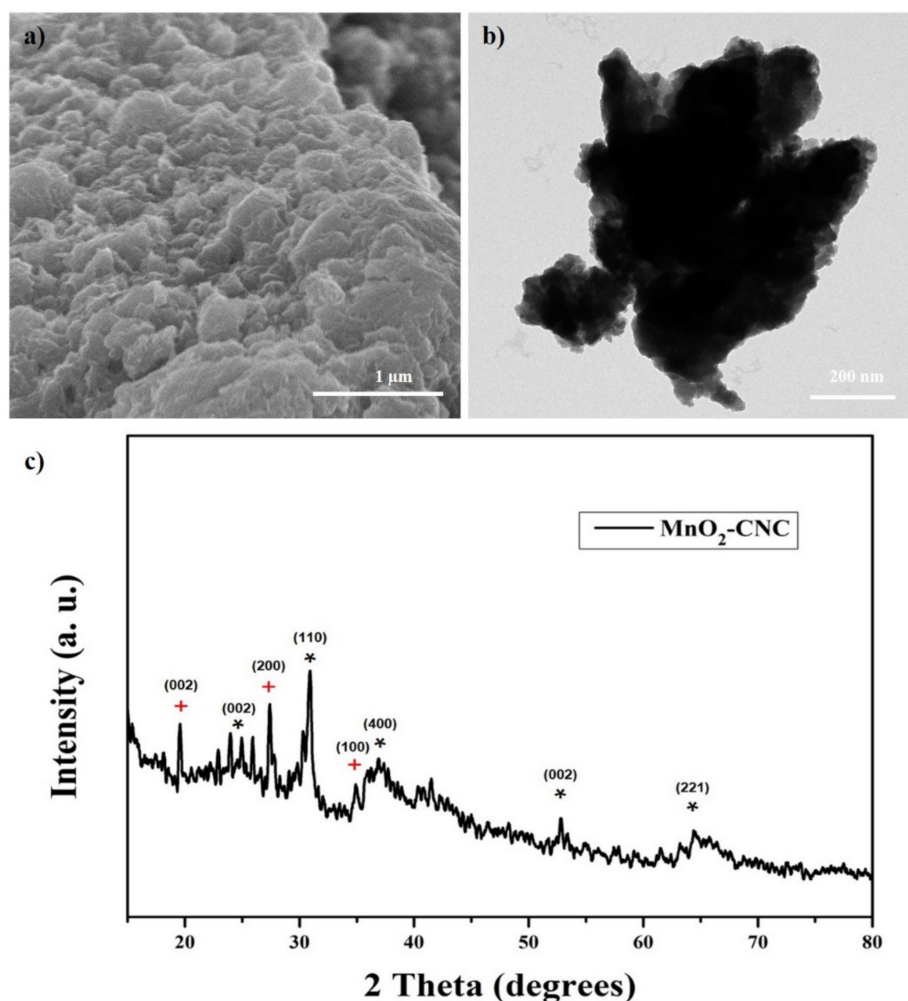


Figure 11. (a) SEM, (b) TEM and (c) XRD patterns of MnO<sub>2</sub>-CNC composite electrodes after 1000 cycles.

In order to compare our research work with previous reports, which employ the nanocomposites of MnO<sub>2</sub> and carbon-based materials working as the LIB anode, the electrochemical performances of LIBs are summarized in Table 1. Several electrically conductive carbon materials, such as carbon nanotube, graphene, and carbon nanohorns, have been used as substrate materials to improve the poor electrical conductivity of MnO<sub>2</sub> and the anode structure stability. The results show that the new nanocomposite made of electrically conductive carbon materials and MnO<sub>2</sub> can deliver a high initial capacity, with some reports exhibiting a better capacity than that of our work for the first 20~50 cycles. However, many of these materials show a significant drop in capacity in following cycles and still suffer from a stable cycle performance. On the other hand, our fabricated nanocomposite not only provides a good initial capacity, but also improves the material electrochemical performance during the extended number of cycles. In addition, the CNC effectively protects the structural stability of the anode material, leading to a better cycle stability.

**Table 1.** Summary of previous works for electrochemical performance employing MnO<sub>2</sub>/electrically conductive carbon material composite.

No.	Composite	Discharge Capacity	Performance Cycle	Current Density	Reference
1.	MnO <sub>2</sub> -CNC	305 mAh g <sup>-1</sup>	1000	100 mA g <sup>-1</sup>	Our work
2.	MOCNF (MnO <sub>2</sub> coated carbon nanofiber)	545 mAh g <sup>-1</sup>	1000	1000 mA g <sup>-1</sup>	[9]
3.	MnO <sub>2</sub> (LMO)/PEDOT/Graphene	948 mAh g <sup>-1</sup>	15	50 mA g <sup>-1</sup>	[25]
4.	Graphene-MnO <sub>2</sub> -GNRs (Graphene nanoribbons)	890 mAh g <sup>-1</sup>	180	100 mA g <sup>-1</sup>	[26]
5.	MnO <sub>2</sub> /CNT hybrid coaxial nanotube	~500 mAh g <sup>-1</sup>	15	50 mA g <sup>-1</sup>	[30]
6.	MnO <sub>2</sub> /PGC (Porous graphitic carbon)	692 mAh g <sup>-1</sup>	400	50 mA g <sup>-1</sup>	[31]
7.	MnO <sub>2</sub> /CNH (Carbon nanohorns)	565 mAh g <sup>-1</sup>	60	100 mA g <sup>-1</sup>	[32]
8.	MnO <sub>2</sub> /CNTs (Carbon Nanotube)	545 mAh g <sup>-1</sup>	1500	240 mA g <sup>-1</sup>	[33]
9.	Graphene/MnO <sub>2</sub>	225 mAh g <sup>-1</sup>	200	50 mA g <sup>-1</sup>	[34]
10.	MnO <sub>2</sub> /CNTs (Carbon Nanotube)	858 mAh g <sup>-1</sup>	260	200 mA g <sup>-1</sup>	[49]
11.	MnO <sub>2</sub> /GDY (Graphdiyne)	660 mAh g <sup>-1</sup>	120	200 mA g <sup>-1</sup>	[50]
12.	MnO <sub>2</sub> @HCN (Hollow carbon nanosphere)	604 mAh g <sup>-1</sup>	200	60 mA g <sup>-1</sup>	[51]

#### 4. Conclusions

In summary, we proposed a successful synthesis of a nanocomposite material of nanosized MnO<sub>2</sub> supported by pyrolyzed nanocrystalline cellulose (CNC). The obtained nanocomposite-based anode exhibited an excellent cycling stability, rate performance, and capacity for LIBs. CNC not only improved the nanostructure by preventing the aggregation of MnO<sub>2</sub>, but also effectively assisted the large volume expansion upon cycling. The pyrolyzed CNC clearly contributed to an enhancement of the electrode performance, especially at high current densities. The obtained electrode shows an average reversible capacity of 193 mAh g<sup>-1</sup> at 10 A g<sup>-1</sup> current. The composite materials exhibited a stably increasing discharge capacity of 305 mAh g<sup>-1</sup> after 1000 cycles and retained 36% of its inception capacity with a Coulombic efficiency of over 99.0% at 100 mA g<sup>-1</sup>. Moreover, the presence of pyrolyzed CNC is confirmed to overcome the drawbacks of nanosized MnO<sub>2</sub> and maintains its structural stability, leading to a better capacity at high current densities, and the stable and excellent long-term cycling performance of nanocomposite as the electrode material of LIBs. Thus, the MnO<sub>2</sub>-CNC nanocomposite is an efficient electrode material for improving the electrochemical performance of next-generation LIBs.

**Author Contributions:** Investigation, Q.N.T.; Formal analysis, T.N.V.; Methodology, I.T.K.; Conceptualization, J.H.K.; Validation, D.H.L.; Writing—Review and Editing, S.J.P. All authors have read and agreed to the published version of the manuscript.

**Funding:** This research was supported by the Basic Science Capacity Enhancement Project through Korea Basic Science Institute (National research Facilities and Equipment Center) grant funded by the Ministry of Education (Grant No. 2019R1A6C1010016) and by the Korea Institute of Energy Technology Evaluation and Planning (KETEP) and the Ministry of Trade, Industry and Energy (MOTIE) of the Republic of Korea (No. 20194030202290).

**Institutional Review Board Statement:** Not applicable.

**Informed Consent Statement:** Not applicable.

**Conflicts of Interest:** The authors declare no conflict of interest.

## References

1. Poizot, P.; Laruelle, S.; Grugeon, S.; Dupont, L.; Tarascon, J.-M. Nano-sized transition-metal oxides as negative-electrode materials for lithium-ion batteries. *Nat. Cell Biol.* **2000**, *407*, 496–499. [[CrossRef](#)] [[PubMed](#)]
2. Jiang, J.; Li, Y.; Liu, J.; Huang, X.; Yuan, C.; Lou, X.W. Recent Advances in Metal Oxide-based Electrode Architecture Design for Electrochemical Energy Storage. *Adv. Mater.* **2012**, *24*, 5166–5180. [[CrossRef](#)] [[PubMed](#)]
3. Zhang, L.; Wu, H.B.; Lou, X.W. Iron-Oxide-Based Advanced Anode Materials for Lithium-Ion Batteries. *Adv. Energy Mater.* **2013**, *4*, 1300958. [[CrossRef](#)]
4. Arnaiz, M.; Botas, C.; Carriazo, D.; Mysyk, R.; Mijangos, F.; Rojo, T.; Ajuria, J.; Goikolea, E. Reduced graphene oxide decorated with SnO<sub>2</sub> nanoparticles as negative electrode for lithium ion capacitors. *Electrochim. Acta* **2018**, *284*, 542–550. [[CrossRef](#)]
5. Yan, L.; Yu, J.; Luo, H. Ultrafine TiO<sub>2</sub> nanoparticles on reduced graphene oxide as anode materials for lithium ion batteries. *Appl. Mater. Today* **2017**, *8*, 31–34. [[CrossRef](#)]
6. Xing, X.; Liu, R.; Liu, S.; Xiao, S.; Xu, Y.; Wang, C.; Wu, D. Surfactant-Assisted Hydrothermal Synthesis of Cobalt Oxide/Nitrogen-Doped Graphene Framework for Enhanced Anodic Performance in Lithium Ion Batteries. *Electrochim. Acta* **2016**, *194*, 310–316. [[CrossRef](#)]
7. Kang, Y.-M.; Song, M.-S.; Kim, J.-H.; Kim, H.-S.; Park, M.-S.; Lee, J.-Y.; Liu, H.K.; Dou, S.X. A study on the charge–discharge mechanism of Co<sub>3</sub>O<sub>4</sub> as an anode for the Li ion secondary battery. *Electrochim. Acta* **2005**, *50*, 3667–3673. [[CrossRef](#)]
8. Chen, Z.; Belharouak, I.; Sun, Y.K.; Amine, K. Titanium-Based Anode Materials for Safe Lithium-Ion Batteries. *Adv. Funct. Mater.* **2012**, *23*, 959–969. [[CrossRef](#)]
9. Park, J.H.; Choi, W.Y.; Lee, S.; Kim, T.-S.; Lee, J.W. Graphene intercalated free-standing carbon paper coated with MnO<sub>2</sub> for anode materials of lithium ion batteries. *Electrochim. Acta* **2020**, *348*, 136310. [[CrossRef](#)]
10. Huang, X.-L.; Wang, R.-Z.; Xu, D.; Wang, Z.-L.; Wang, H.-G.; Xu, J.-J.; Wu, Z.; Liu, Q.-C.; Zhang, Y.; Zhang, X. Homogeneous CoO on Graphene for Binder-Free and Ultralong-Life Lithium Ion Batteries. *Adv. Funct. Mater.* **2013**, *23*, 4345–4353. [[CrossRef](#)]
11. Lu, Y.; Yu, L.; Lou, X.W. Nanostructured Conversion-type Anode Materials for Advanced Lithium-Ion Batteries. *Chem* **2018**, *4*, 972–996. [[CrossRef](#)]
12. Míhira, A.; Mehta, A.; Basu, S.; Malode, S.J.; Shetti, N.P.; Shukla, S.S.; Nadagouda, M.N.; Aminabhavi, J.M. Electrode materials for lithium-ion batteries. *Mater. Sci. Technol.* **2018**, *1*, 182–187.
13. Nitta, N.; Wu, F.; Lee, J.T.; Yushin, G. Li-ion battery materials: Present and future. *Mater. Today* **2014**, *18*, 252–264. [[CrossRef](#)]
14. Xing, Z.; Wang, B.; Halsted, J.K.; Subashchandrabose, R.; Stickle, W.F.; Ji, X. Direct fabrication of nanoporous graphene from graphene oxide by adding a gasification agent to a magnesiothermic reaction. *Chem. Commun.* **2014**, *51*, 1969–1971. [[CrossRef](#)]
15. Xing, Z.; Lu, J.; Ji, X. A Brief Review of Metallothermic Reduction Reactions for Materials Preparation. *Small Methods* **2018**, *2*, 1800062. [[CrossRef](#)]
16. Gu, X.; Yue, J.; Li, L.; Xue, H.; Yang, J.; Zhao, X. General Synthesis of MnO<sub>x</sub> (MnO<sub>2</sub>, Mn<sub>2</sub>O<sub>3</sub>, Mn<sub>3</sub>O<sub>4</sub>, MnO) Hierarchical Microspheres as Lithium-ion Battery Anodes. *Electrochim. Acta* **2015**, *184*, 250–256. [[CrossRef](#)]
17. Chen, J.; Wang, Y.; He, X.; Xu, S.; Fang, M.; Zhao, X.; Shang, Y. Electrochemical properties of MnO<sub>2</sub> nanorods as anode materials for lithium ion batteries. *Electrochim. Acta* **2014**, *142*, 152–156. [[CrossRef](#)]
18. Shin, J.; Seo, J.K.; Yaylian, R.; Huang, A.; Meng, Y.S. A review on mechanistic understanding of MnO<sub>2</sub> in aqueous electrolyte for electrical energy storage systems. *Int. Mater. Rev.* **2019**, *65*, 356–387. [[CrossRef](#)]
19. Gao, F.; Qin, S.-H.; Zang, Y.-H.; Gu, J.-F.; Qu, J.-Y. Highly efficient formation of Mn<sub>3</sub>O<sub>4</sub>-graphene oxide hybrid aerogels for use as the cathode material of high performance lithium ion batteries. *New Carbon Mater.* **2020**, *35*, 121–130. [[CrossRef](#)]
20. Kokubu, T.; Oaki, Y.; Hosono, E.; Zhou, H.; Imai, H. Biomimetic Solid-Solution Precursors of Metal Carbonate for Nanostructured Metal Oxides: MnO/Co and MnO-CoO Nanostructures and Their Electrochemical Properties. *Adv. Funct. Mater.* **2011**, *21*, 3673–3680. [[CrossRef](#)]
21. Lowe, M.A.; Gao, J.; Abruña, H.D. In operando X-ray studies of the conversion reaction in Mn<sub>3</sub>O<sub>4</sub> lithium battery anodes. *J. Mater. Chem. A* **2012**, *1*, 2094–2103. [[CrossRef](#)]
22. Qiu, Y.; Xu, G.-L.; Yan, K.; Sun, H.; Xiao, J.; Yang, S.; Sun, S.-G.; Jin, L.; Deng, H. Morphology-conserved transformation: Synthesis of hierarchical mesoporous nanostructures of Mn<sub>2</sub>O<sub>3</sub> and the nanostructural effects on Li-ion insertion/deinsertion properties. *J. Mater. Chem.* **2011**, *21*, 6346–6353. [[CrossRef](#)]
23. Tao, J.; Liu, N.; Ma, W.; Ding, L.; Li, L.; Su, J.; Gao, Y. Solid-State High Performance Flexible Supercapacitors Based on Polypyrrole-MnO<sub>2</sub>-Carbon Fiber Hybrid Structure. *Sci. Rep.* **2013**, *3*, 2286. [[CrossRef](#)]
24. Xu, G.-L.; Xu, Y.-F.; Sun, H.; Fu, F.; Zheng, X.-M.; Huang, L.; Li, J.-T.; Yang, S.-H.; Sun, S.-G. Facile synthesis of porous MnO/C nanotubes as a high capacity anode material for lithium ion batteries. *Chem. Commun.* **2012**, *48*, 8502–8504. [[CrossRef](#)] [[PubMed](#)]
25. Guo, C.X.; Wang, M.; Chen, T.; Lou, X.W.; Li, C.M. A Hierarchically Nanostructured Composite of MnO<sub>2</sub>/Conjugated Polymer/Graphene for High-Performance Lithium Ion Batteries. *Adv. Energy Mater.* **2011**, *1*, 736–741. [[CrossRef](#)]

26. Li, L.; Raji, A.-R.O.; Tour, J.M. Graphene-Wrapped MnO<sub>2</sub>-Graphene Nanoribbons as Anode Materials for High-Performance Lithium Ion Batteries. *Adv. Mater.* **2013**, *25*, 6298–6302. [[CrossRef](#)]
27. Yue, J.; Gu, X.; Chen, L.; Wang, N.; Jiang, X.; Xu, H.; Yang, J.; Qian, Y. General synthesis of hollow MnO<sub>2</sub>, Mn<sub>3</sub>O<sub>4</sub> and MnO nanospheres as superior anode materials for lithium ion batteries. *J. Mater. Chem. A* **2014**, *2*, 17421–17426. [[CrossRef](#)]
28. Antonino, S.A.; Peter, B.; Bruno, S.; Jean-Marie, T. Nanostructured materials for advanced energy conversion and storage devices. *Nat. Mater.* **2005**, *4*, 366–377.
29. Dias, G.M.V.; Müller, D.; Wesling, B.; Bernardes, J.C.; Hotza, D.; Rambo, C.R. Enhancing Specific Capacitance and Cyclic Stability through Incorporation of MnO<sub>2</sub> into Bacterial Nanocellulose/PPy-CuCl<sub>2</sub> Flexible Electrodes. *Energy Technol.* **2019**, *7*, 1900328. [[CrossRef](#)]
30. Kundu, M.; Singh, G.; Svensson, A.M. Co(OH)<sub>2</sub>@MnO<sub>2</sub> nanosheet arrays as hybrid binder-free electrodes for high-performance lithium-ion batteries and supercapacitors. *New J. Chem.* **2018**, *43*, 1257–1266. [[CrossRef](#)]
31. Zeng, H.; Xing, B.; Zhang, C.; Chen, L.; Zhao, H.; Han, X.; Yi, G.; Huang, G.; Zhang, C.; Cao, Y. In Situ Synthesis of MnO<sub>2</sub>/Porous Graphitic Carbon Composites as High-Capacity Anode Materials for Lithium-Ion Batteries. *Energy Fuels* **2020**, *34*, 2480–2491. [[CrossRef](#)]
32. Lai, H.; Li, J.; Chen, Z.; Huang, Z. Carbon Nanohorns As a High-Performance Carrier for MnO<sub>2</sub> Anode in Lithium-Ion Batteries. *ACS Appl. Mater. Interfaces* **2012**, *4*, 2325–2328. [[CrossRef](#)] [[PubMed](#)]
33. Zhang, X.; Wang, T.; Jiang, C.; Zhang, F.; Li, W.; Tang, Y. Manganese Dioxide/Carbon Nanotubes Composite with Optimized Microstructure via Room Temperature Solution Approach for High Performance Lithium-Ion Battery Anodes. *Electrochim. Acta* **2016**, *187*, 465–472. [[CrossRef](#)]
34. Cetinkaya, T.; Tokur, M.; Ozcan, S.; Uysal, M.; Akbulut, H. Graphene supported  $\alpha$ -MnO<sub>2</sub> nanocomposite cathodes for lithium ion batteries. *Int. J. Hydrog. Energ.* **2016**, *41*, 6945–6953. [[CrossRef](#)]
35. Reddy, A.L.M.; Shaijumon, M.; Gowda, S.R.; Ajayan, P.M. Coaxial MnO<sub>2</sub>/Carbon Nanotube Array Electrodes for High-Performance Lithium Batteries. *Nano Lett.* **2009**, *9*, 1002–1006. [[CrossRef](#)]
36. Rakhi, R.B.; Cha, N.; Chen, W.; Alshareef, H.N. Electrochemical Energy Storage Devices Using Electrodes Incorporating Carbon Nanocoils and Metal Oxides Nanoparticles. *J. Phys. Chem. C* **2011**, *115*, 14392–14399. [[CrossRef](#)]
37. Yuan, D.; Zhang, T.; Guo, Q.; Qiu, F.; Yang, D.; Ou, Z. Recyclable biomass carbon@SiO<sub>2</sub>@MnO<sub>2</sub> aerogel with hierarchical structures for fast and selective oil-water separation. *Chem. Eng. J.* **2018**, *351*, 622–630. [[CrossRef](#)]
38. Su, D.; Pan, L.; Fu, X.; Ma, H. Facile synthesis of CNC-MnO<sub>2</sub> hybrid as a supercapacitor electrode. *Appl. Surf. Sci.* **2015**, *324*, 349–354. [[CrossRef](#)]
39. Wang, Z.; Pan, R.; Sun, R.; Edström, K.; Strømme, M.; Nyholm, L. Nanocellulose Structured Paper-Based Lithium Metal Batteries. *ACS Appl. Energy Mater.* **2018**, *1*, 4341–4350. [[CrossRef](#)]
40. Tran, Q.N.; Kim, I.T.; Park, S.; Choi, H.W.; Park, S.J. SnO<sub>2</sub> Nanoflower–Nanocrystalline Cellulose Composites as Anode Materials for Lithium-Ion Batteries. *Materials* **2020**, *13*, 3165. [[CrossRef](#)] [[PubMed](#)]
41. Xia, H.; Lai, M.; Lu, L. Nanoflaky MnO<sub>2</sub>/carbon nanotube nanocomposites as anode materials for lithium-ion batteries. *J. Mater. Chem.* **2010**, *20*, 6896–6902. [[CrossRef](#)]
42. Yang, J.; Wang, S.; Ma, Z.; Du, Z.; Li, C.; Song, J.; Wang, G.; Shao, G. Novel nitrogen-doped hierarchically porous coralloid carbon materials as host matrixes for lithium–sulfur batteries. *Electrochim. Acta* **2015**, *159*, 8–15. [[CrossRef](#)]
43. He, J.; Zhao, S.; Lian, Y.; Zhou, M.; Wang, L.; Ding, B.; Cui, S. Graphene-doped carbon/Fe<sub>3</sub>O<sub>4</sub> porous nanofibers with hierarchical band construction as high-performance anodes for lithium-ion batteries. *Electrochim. Acta* **2017**, *229*, 306–315. [[CrossRef](#)]
44. De las Casas, C.; Li, W. A review of application of carbon nanotubes for lithium ion battery anode material. *J. Power Sources* **2012**, *208*, 74–85. [[CrossRef](#)]
45. Cai, Z.; Xu, L.; Yan, M.; Han, C.; He, L.; Hercule, K.M.; Niu, C.; Yuan, Z.; Xu, W.; Qu, L.; et al. Manganese Oxide/Carbon Yolk–Shell Nanorod Anodes for High Capacity Lithium Batteries. *Nano Lett.* **2014**, *15*, 738–744. [[CrossRef](#)] [[PubMed](#)]
46. Lou, X.W.; Chen, J.S.; Chen, P.; Archer, L.A. One-Pot Synthesis of Carbon-Coated SnO<sub>2</sub> Nanocolloids with Improved Reversible Lithium Storage Properties. *Chem. Mater.* **2009**, *21*, 2868–2874. [[CrossRef](#)]
47. Lian, P.; Zhu, X.; Liang, S.; Li, Z.; Yang, W.; Wang, H. High reversible capacity of SnO<sub>2</sub>/graphene nanocomposite as an anode material for lithium-ion batteries. *Electrochim. Acta* **2011**, *56*, 4532–4539. [[CrossRef](#)]
48. Wang, L.; Yu, Y.; Chen, P.; Zhang, D.; Chen, C. Electrospinning synthesis of C/Fe<sub>3</sub>O<sub>4</sub> composite nanofibers and their application for high performance lithium-ion batteries. *J. Power Sources* **2008**, *183*, 717–723. [[CrossRef](#)]
49. Wu, Y.; Li, X.; Xiao, Q.; Lei, G.; Li, Z.; Guan, J. The coaxial MnO<sub>2</sub>/CNTs nanocomposite freestanding membrane on SSM substrate as anode materials in high performance lithium ion batteries. *J. Electroanal. Chem.* **2019**, *834*, 161–166. [[CrossRef](#)]
50. Lin, Y.; Kang, H.; Liang, M.; Ye, X.; Li, J.; Feng, Q.; Zheng, Y.; Huang, Z. Hybrid nanostructured MnO<sub>2</sub> nanowire/graphdiyne with enhanced lithium-ion performance promoting by interfacial storage. *Appl. Surf. Sci.* **2020**, *526*, 146457. [[CrossRef](#)]
51. Cao, Z.; Yang, Y.; Qin, J.; Su, Z. A core-shell porous MnO<sub>2</sub>/Carbon nanosphere composite as the anode of lithium-ion batteries. *J. Power Sources* **2021**, *491*, 229577. [[CrossRef](#)]